Research

Author for correspondence:
Gwennou Coupier
e-mail:
gwennou.coupier@univ-grenoble-alpes.fr

Post-buckling dynamics of spherical shells

Marcel Mokbel[1,2], Adel Djellouli[3,4], Catherine Quilliet[3], Sebastian Aland[1,2] and Gwennou Coupier[3]

[1]University of Applied Sciences (HTW) Dresden, Friedrich-List-Platz 1, 01069 Dresden, Germany
[2]Technische Universität Bergakademie Freiberg, Akademiestrasse, 609599 Freiberg, Germany
[3]Université Grenoble Alpes, CNRS, LIPhy, 38000 Grenoble, France
[4]School of Engineering and Applied Sciences Cambridge, Harvard University, Cambridge, MA 02138, USA

GC, 0000-0001-5010-4148

We explore the intrinsic dynamics of spherical shells immersed in a fluid in the vicinity of their buckled state, through experiments and three-dimensional axisymmetric simulations. The results are supported by a theoretical model that accurately describes the buckled shell as a two-variable-only oscillator. We quantify the effective 'softening' of shells above the buckling threshold, as observed in recent experiments on interactions between encapsulated microbubbles and acoustic waves. The main dissipation mechanism in the neighbouring fluid is also evidenced.

1. Introduction

Buckling of elastic structures has recently emerged as a powerful mechanism to trigger fast motion at small scale. This includes fast reorientation of microswimmers [1,2], thrust generation in fluids [3,4] or, through solid friction [5], valves actuation for flow control [6,7] or fast actuation of optical lenses [8]. Smart design of materials in order to obtain the desired buckling behaviour has now become an intense field of research [9–12].

From a modelling perspective, stable configurations of structures prone to buckling have been widely explored, as well as the stress or strain thresholds that have to be overcome to switch between states. The existence of (at least) two stable states separated by energy barriers allows for the design of robust devices that can maintain their state within a certain range of external perturbation without any external energy input. While the picture in

terms of equilibrium states is now quite clear, at least for simple geometries (rods, half-spheres, closed spheres), full control of soft structures by external signals requires to know more about their dynamics. Recent papers have shed light on the complexity of the first-stage dynamics, close to the buckling threshold, where the response time of the material depends on classical dissipative mechanisms coupled to intrinsic slowing down observed in such a critical phenomenon [13–15]. The goal of the present paper is to explore the second-stage dynamics, around the buckled state, where the geometry is often more complex than that of the initial state.

Because of their ubiquitousness in nature but also of their simplicity in terms of fabrication and of modelling, spherical closed shells enclosing a compressible fluid are particularly in the spotlight [3,16–30]. Existing studies are essentially focused on understanding the scenario of the buckling instability that occurs beyond a certain threshold of compression or deflation, and on characterizing the stability branches [22,24,25,29]. More recently, shells made of non-isotropic material have also attracted some attention [31–33]. In terms of dynamics, the reaction of shells to a steep increase of pressure have been recently studied [15,34], while an experimental study has highlighted the role of dissipation within the shell while reaching the stable buckled state [29].

Hollow microshells have been used for decades as ultrasound contrast agents (UCAs), and their resonance frequencies in the spherical configuration have been widely studied [35]. Noteworthy, even in such a simple configuration, the existing models lack to describe accurately all experimental observations [36]. Depending on the applied acoustic field, UCAs may also buckle. In [37], the current state of a suspension of UCAs is controlled by a low-frequency acoustic field while the propagation velocity of a high-frequency acoustic signal is measured. The authors observe a decrease of this sound speed while the ambient pressure is increased above a certain threshold, in marked contrast with the standard results in a simple fluid. As in other preceding works [38,39], this is interpreted as a 'softening' of the shell due to its buckling. This interpretation is consolidated by the existence of a hysteretic loop as the ambient pressure is varied, which is also a signature of the buckling–unbuckling transitions. A very different study reaches the same conclusion: in [40], primary Bjerkness forces on hollow micrometric shells are measured; a strong rise of this force above a given amplitude of the applied acoustic field is interpreted again as a signature of the sudden 'softening' of the shell. This interpretation is supported by independent measurements of the buckling pressure by AFM.

In all the above-mentioned studies, the data are not quantitatively fitted by a model. Indeed, to our knowledge, the sole model accounting for shell response in the buckled state is that of Marmottant *et al.* [41], which has been refined in [42]. These models assume that in the buckled configuration, the elastic response of the whole shell is simply that of the encapsulated gas while that due to shell material has disappeared, as if the shell was broken.

In the present work, we show that this rough approach is not valid. While our results confirm the effective softening due to buckling, we highlight a more complex interplay between gas response and shell material response, reaching the unexpected result that softening is even more pronounced than that obtained through neglecting shell material response.

2. Statement of the problem

(a) Description of relevant parameters

We consider spherical elastic shells made of an isotropic, incompressible elastic material of Young's modulus E and initial thickness d. We have performed experiments on home-made shells of centimetric size (see appendix A), which allowed checking the consistency of our numerical simulations where the different relevant parameters could be varied on a wider range. In these simulations, we consider isolated zero-thickness elastic shells of initial radius R_0 whose elastic constants (compression and curvature modulus) are functions of E and d (see appendix B). These shells are immersed in a Newtonian fluid in which the Navier–Stokes equation is solved. They are filled with a gas at pressure P that is assumed to be instantaneously set by the shell volume according to an adiabatic process, a reasonable hypothesis considering the high velocities

encountered in this problem: $PV^\kappa = P_0 V_0^\kappa$, where V is the shell volume, V_0 its initial value, P_0 the initial pressure and κ is the polytropic coefficient. While the fabrication process of shells makes it difficult to obtain a measurable initial pressure other than the atmospheric one, the simulations have allowed to vary it so as to explore the relative contributions of gas compressibility and shell elasticity on the overall response. The thin shell limit that is considered here, though it may appear as a strong simplification, is indeed a relevant model even to describe thick shells, as evoked in [29] and confirmed in the following. The ambient pressure is initially equal to P_0 and is suddenly increased to a constant value P_{ext}, which is large enough to trigger buckling.

The large range of parameters we consider here will allow us to establish post-buckling dynamics for a wide range of objects and scales, from the thin colloidal shells that are used, in particular, as UCAs [41,43–45] or photoacoustics contrast agents [46], to macroscopic shells in elastomer, which are among the favourite building blocks in soft robotics [3,5,9].

To describe this whole range, we consider the dimensionless problem obtained by considering the shell radius R_0 as the lengthscale (its mid-plane radius for a real shell), Ed/R_0 as the pressure and elastic modulus scale, and ρ_f as the density scale. The time scale is then $\sqrt{\rho_f R_0^3/(Ed)}$. This scaling is that of the undamped period of an oscillating shell when the contribution of inner pressure is neglected.

The problem now depends on four parameters: the reduced thickness of the shell $\hat{d} = d/R_0$, the initial pressure $\hat{P}_0 = P_0/(Ed/R_0)$ in the shell when it is in its stress-free spherical configuration, the applied pressure $\hat{P}_{\text{ext}}$ and the dimensionless viscosity of the fluid $\hat{\eta} = \eta_f/\sqrt{Ed\rho_f R_0}$ that will characterize the damping in the system. This last number is the equivalent of an Ohnesorge number where surface tension has been replaced by the two-dimensional elastic modulus Ed. We detail in table 1 the typical values of the three parameters $\hat{d}$, $\hat{P}_0$ and $\hat{\eta}$ (characterizing the initial state) one may find when considering microshells and macroshells used within the current research context, as well as the range covered by our experiments and simulations.

Both in numerical simulations [22,24,26] or in experiments [29], it is now well established that at equilibrium, the pressure difference $P_{\text{ext}} - P$ quasi-plateaus to a constant ΔP_{pl} as a function of equilibrium volumes V_e. Therefore, varying the fourth parameter $\hat{P}_{\text{ext}}$ strictly amounts to varying the equilibrium pressure $\hat{P}_e$ inside the shell, which we already set here by varying the initial pressure. In our experiments and simulations, $\hat{P}_{\text{ext}}$ is typically chosen such that the pressure difference is right above the buckling threshold $\Delta \hat{P}_b = 4\hat{d}/3$ [22,26]. Increasing too much the external pressure, or starting with very low pressure inside the shell, leads to a full collapse of the shell, with the two opposite poles being in contact. This pertains to a new kind of physics taking into account solid friction and requires additional development in the numerical method. We will avoid these extreme situations in the present work.

In the following, we will often discuss the effect of the four control parameters by varying them from a reference configuration (also chosen for figures 1 and 2), named $\mathcal{R}$ hereafter, where $\hat{d} = 0.22$, $\hat{P}_0 = 0.9$, $\hat{\eta} = 0.004$ and $\hat{P}_{\text{ext}} = 1.6$. This corresponds, for example, to a macroscopic situation, where $\eta = 1\,\text{Pa}\cdot\text{s}$ (e.g. glycerol), $R_0 = 22.5\,\text{mm}$, $d = 5\,\text{mm}$, $E = 0.5\,\text{MPa}$, $P_0 = 1\,\text{bar}$ and $P_{\text{ext}} = 1.77$ bar (figure 1), or to a microscopic configuration with the same pressures and elastic modulus and $\eta = 1\,\text{mPa}\cdot\text{s}$ (e.g. water), $R_0 = 22.5\,\mu\text{m}$ and $d = 5\,\mu\text{m}$.

(b) A 2-frequency oscillator

In the experiments as in the simulations, we consider the dynamics of a shell that is brought to the onset of buckling by setting the external pressure P_{ext} to a value determined by a preliminary study. The external pressure is then kept fixed at this value and the dynamics of deformation of the shell is recorded. The sudden collapse of a shell at the buckling transition is followed by oscillations around the new equilibrium position. We show in figure 1 the oscillations of two geometrical characteristics of a shell in configuration $\mathcal{R}$, corresponding to one of our experiments. A noticeable effect is the apparition of a second frequency in the oscillation pattern; moreover, in

Table 1. Some orders of magnitude for two typical objects of interest: ultrasound contrast agents (UCAs) [35,36] and polymeric macroscopic shells [3,5]. Initial inner pressure in UCAs is often assumed to be close to atmospheric pressure while it may be varied on purpose in macroscopic shells. The ranges of parameters covered by the present experiments and simulations are also indicated. See text for the definition of the dimensionless parameters (hatted symbols).

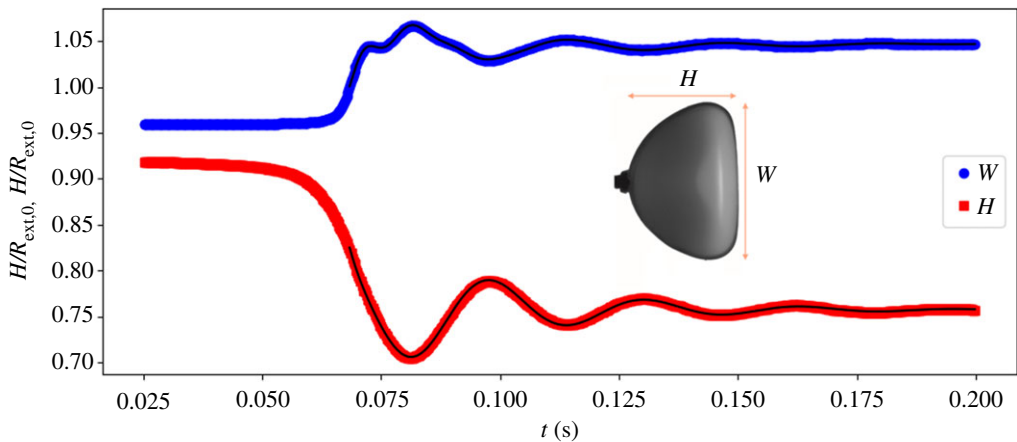| shell type	R_0 (mm)	d	E (MPa)	P_0 (MPa)	ρ_f (kg m^{-3})	η_f (mPa·s)	$\hat{d}(\times 10^{-3})$	$\hat{P}_0$	$\hat{\eta}(\times 10^{-3})$
UCA	0.001–0.005	2–5 nm	1–100	0.1	1000	1	0.4–5	0.2–250	20–700
macroshell	1–100	$0.01 - 0.5\,R_0$	0.01–1	0.1–10	1000	1–1000	10–500	$0.2-10^5$	0.004–3000
experiments	6.75–67.5	$0.08-0.3\,R_0$	0.5	0.1	1260	1000	80–300	0.7–2.5	1.3–13
simulations							40–300	0.2–5	0.6–1300

Figure 1. Oscillations of the width W and height H of the convex envelope of a shell with external radius $R_{ext,0} = 25$ mm, thickness $d = 5$ mm, Young's modulus $E = 0.5$ MPa, initial internal pressure $P_0 = 1$ bar, external pressure $P_{ext} = 1.77$ bar, immersed in glycerol (experiments in the reference configuration $\mathcal{R}$). Black lines correspond to the fit by the sum of two damped sinusoidal functions, which are obviously necessary to recover the full curve for the width W. The two frequencies are of the order 30 and 90 Hz, and are much lower than that typical of spherical configuration, which is $f = (1/2\pi R_0)\sqrt{(1/\rho_f)(3\kappa P_0 + 4Ed/R_0)} \sim 210$ Hz (e.g. [41]). Here R_0 is the mid-plane radius $R_{ext,0} - d/2$. Note that the sole gas contribution leads to a Minnaert frequency $(1/2\pi R_0)\sqrt{3\kappa P_0/\rho_f} \sim 140$ Hz, which is also larger than the observed frequencies. These observations call for a finer modelling of the oscillation mechanisms around the buckled state. (Online version in colour.)

agreement with the widely admitted softening of buckled shells, these two frequencies are much lower than that typical of the spherical state.

The apparition of a second frequency invalidates the previous models where the oscillations come from the sole contribution of gas compressibility. Note that we cannot expect more complex behaviour, like the apparition of a second frequency, to emerge from a bubble yet having a non-spherical shape: it has been shown recently [47], in agreement with [48], that the generalized Minnaert model, where the radius of the spherical bubble is replaced by the effective radius extracted from the volume, is robust against geometry changes.

In the experiments, buoyancy issues have required to restrict the displacement of the shell, which was attached to a fixed support through a suction pad located at the pole opposite to the buckling pole. In order to build up a general view of the oscillation mechanism devoid of any suspicion of strong influence of the boundary conditions, we turn to the numerical simulations, which allow to consider free shells and a larger range of parameters. We shall come back in §5d to the impact of having a part of the shell that is fixed.

3. Post-buckling oscillations of a free shell

We illustrate in figure 2 the buckling process as obtained from the simulations. From the many available data characterizing the shell shape, we focus on its volume V and surface S and plot in figure 3 their oscillations towards their equilibrium values V_e and S_e. The drop in volume is all the more pronounced as the initial pressure is low. By contrast, the shell surface increases along the buckling process, and reaches a value close to the initial value of the sphere, which hardly depends on the initial pressure. This validates the vision of the buckling process as a mechanism that makes the shell switch from a spherically compressed state to a more favourable state where the in-plane compression energy is released, the cost to pay being the curvature energy, which is localized in the rim [19].
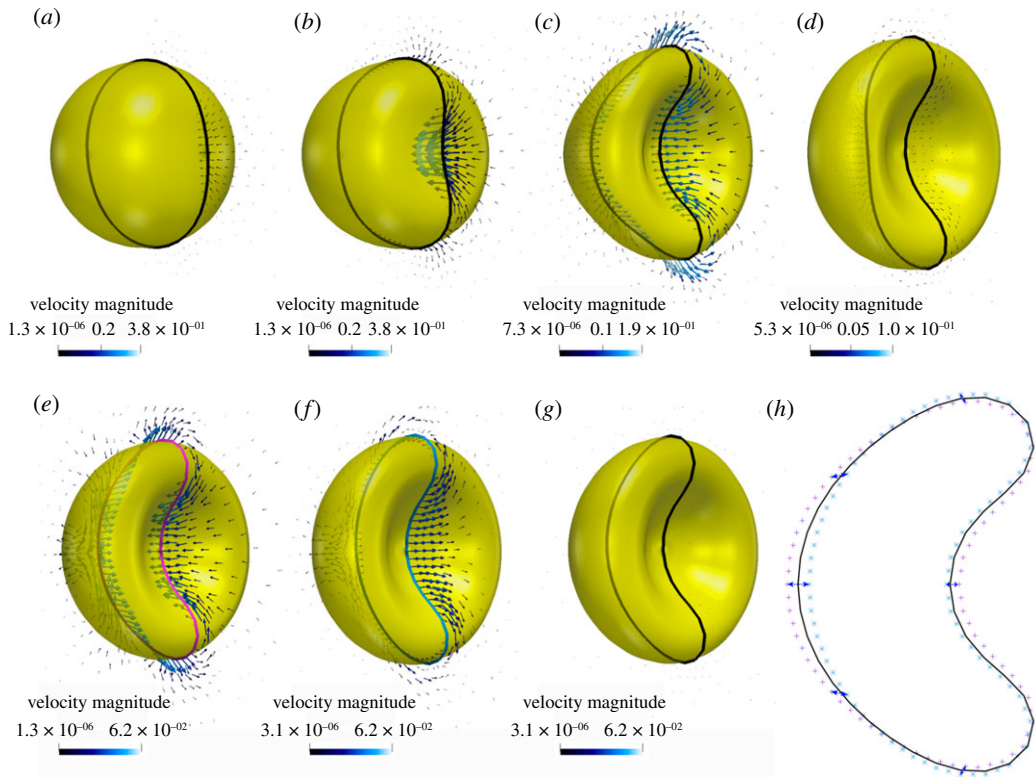
Figure 2. Images of the buckling process from the simulations. The corresponding times are indicated in figure 3a. The arrows refer to the fluid velocity, scaled by the velocity magnitude. (a–d): buckling process, until the buckling spot reaches its deepest spot and the buckling oscillations around the equilibrium state set in. Two of these oscillating configurations are shown in (e–f). (g) is the final equilibrium state. (h) shows the respective contour of the shell, where the purple plus symbols refer to the shape shown in (e) (illustrated by the purple shell contour), the asterisks refer to (f) (illustrated by the blue shell contour) and the black line to (g). The arrows indicate the movement of the surface grid points. The arrows in (e–g) are scaled four times larger than in (a–d) for visualization purposes. See also the corresponding movie in the electronic supplementary materials. (Online version in colour.)

Right after the buckling transition, the signals are, as in the experiments, well fitted by the sum of two sinusoidal functions damped by the same decreasing exponential, as shown in figure 3b. For each simulation, we then obtain three characteristic parameters of the shell dynamics: two frequencies ω_- and ω_+, with $\omega_- < \omega_+$, and a single relaxation time τ. We define $\omega_\pm$ as the intrinsic frequency, obtained from the measured frequency $\Omega_\pm$ through $\omega_\pm^2 = \Omega_\pm^2 + 1/\tau^2$. These three parameters are similar for both V and S, as well as for other characteristic parameters such as the width or the height of the shell (as discussed with figure 9 further in the text). They all depend, *a priori*, on the four control parameters of the problem. In all the simulations we considered, the contribution of the highest frequency to the signal is between 50% and 80% smaller than that of the lowest frequency. We shall then focus first on this latter. In figure 4, we show how this frequency ω_- varies with some control parameters, starting from the reference configuration $\mathcal{R}$. In figure 4a, the initial pressure $\hat{P}_0$ is kept fixed and the external pressure is set right above the threshold for buckling, and the dependency with space parameters is explored. Decreasing the thickness d of a shell of given radius leads to the intuitive result that the frequency decreases, as a result of the decrease of the shell elasticity. For a given reduced thickness $\hat{d}$, figure 4a shows that the reduced frequency does not vary significantly for small enough values of the reduced viscosity $\hat{\eta}$. When damping becomes more important, the frequency decreases, illustrating the threshold at which viscous stresses start to influence the dynamics of the shell beyond a mere linear damping.
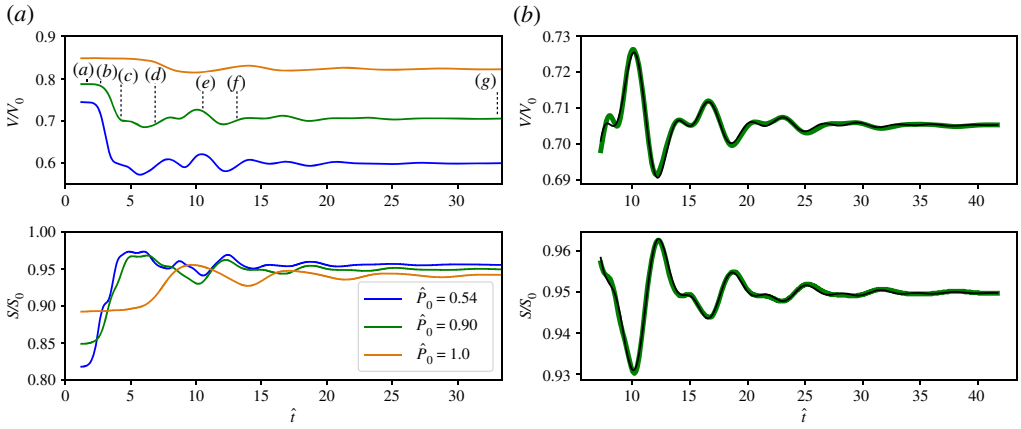
Figure 3. (a) Oscillations of the volume V and surface S of a shell in configuration $\mathcal{R}$ ($\hat{P}_0 = 0.9$) and two other initial pressures (simulations). Letters indicate the times at which the snapshots of figure 2 were taken. V_0 and S_0 are the initial values of the shell volume and surface, respectively. (b) Thin black line : fit of the time evolution of V and S after the buckling stage for a shell in configuration $\mathcal{R}$, by the sum of two sinusoidal functions damped by the same decreasing exponential function. For both V and S, the frequencies are similar. (Online version in colour.)
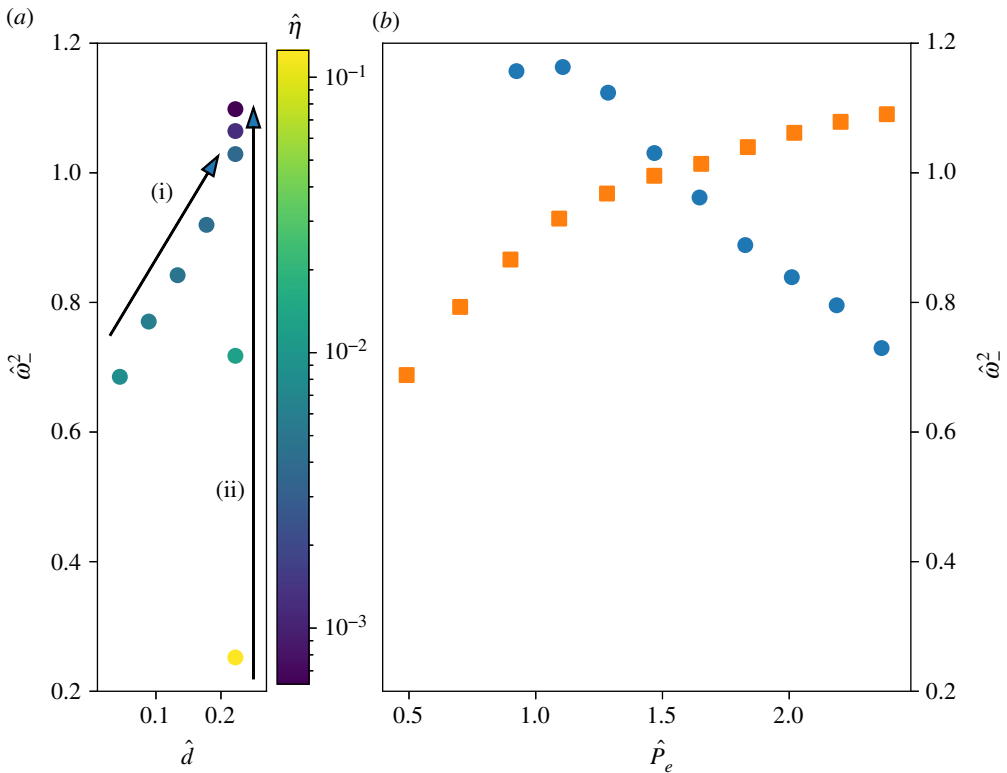

Figure 4. Main pulsation ω_- as a function of some control parameters. From the reference configuration $\mathcal{R}$ ($\hat{d} = 0.22$, $\hat{P}_0 = 0.9$, $\hat{\eta} = 0.004$), one parameter is varied at a time. (a) Following (i): effect of varying d: $\hat{d}$ therefore varies but also $\hat{\eta}$ (see colourbar). Following (ii): effect of varying R_0 at fixed $\hat{d}$ (thus $\hat{\eta}$). (b) Effect of varying $\hat{P}_0$ at fixed $\hat{P}_{ext} - \hat{P}_0$ (blue disks) or $\hat{P}_0$ with $\hat{P}_{ext}$ set such that the final shape is preserved whatever the initial pressure (orange squares). (Online version in colour.)

Less intuitive is the variation of the frequency with the equilibrium pressure inside the shell, shown in figure 4*b*. Starting from shell in configuration $\mathcal{R}$, we varied the initial pressure $\hat{P}_0$ from 0.36 to 1.8. The resulting equilibrium pressure $\hat{P}_e$ increases conjointly with this initial pressure. The result is that in the meantime, the frequency decreases. One can question this observation by extrapolating, in a first approach, that the contribution of the gas to the frequency would scale like the Minnaert frequency ω_M of a free spherical bubble: $\omega_M^2 \propto P_e/V_e^{3/2}$, where we have simply replaced the usual radius of the original Minnaert expression by a generalized radius based on the volume, as in [47,48]. Since the volume at equilibrium V_e is an increasing function of internal pressure P_e, it is not clear *a priori* that the Minnaert frequency increases with pressure. In the spherical case, it can however be calculated that $V_e^{3/2}$ does not increase as quickly as P_e. In our case of buckled configuration, data from the simulations show also that such a Minnaert contribution increases with the equilibrium (or the initial) pressure. Therefore, the origin of the decrease of ω_- with increasing internal pressure has to be found elsewhere.

In order to separate the direct effect of pressure on compressibility from its indirect effect through its influence on the shell volume, it is insightful to consider the following configuration: from the reference configuration $\mathcal{R}$ in its buckled equilibrium state, we have varied the inner and external pressure by the same amount $\delta\hat{P}$, which does not modify the shape of the shell. Then, using this state as the reference state for inner pressure calculation (i.e. $\hat{P}\hat{V}^\kappa = (\hat{P}_e + \delta\hat{P})\hat{V}_e^\kappa$), we apply a small perturbation to the shell and measure the induced oscillations, thus characterizing the pressure contribution to the elastic response, at fixed geometry. As shown in figure 4*b*, while this contribution is now increasing with the pressure, this increase of the frequency squared with the inner pressure is sublinear, in contrast with the spherical case. Note that the procedure amounts to vary $\hat{P}_{\text{ext}}$ together with $\hat{P}_0$ such that the final shape is the same in all simulations. We checked, for a zero offset $\delta\hat{P}$, that these oscillations with small amplitudes are similar to that obtained right after the shell has buckled, which initially implies larger deformations. This can be seen by the proximity between the two data points for $\hat{P}_e \simeq 1.5$ in figure 4*b*.

In order to decipher these behaviours, we introduce a reduced model, which is then used to fit the dataset obtained from the simulations.

4. Model

We describe the dynamics of the system through Lagrangian mechanics, which is an energy approach that allows to introduce the generalized coordinates that are the more relevant to the problem (see [49] for such an approach in the case of spherical oscillations).

In this frame, the dynamics is given by

$$\frac{\mathrm{d}}{\mathrm{d}t}\frac{\partial L}{\partial \dot{q}_i} - \frac{\partial L}{\partial q_i} = -\frac{\partial D}{\partial \dot{q}_i}. \tag{4.1}$$

The Lagrangian function L is defined as $L = T - U$ with T and U the kinetic and potential energies of the system, respectively. The Rayleigh dissipative function D allows to introduce non-conservative forces in the formalism, providing they originate from viscous friction and that pressure drag is negligible. We shall see later that, due to the high buckling velocities, this assumption is fragile. The q_i and $\dot{q}_i$ are the generalized coordinates and velocities that characterize the state of the system.

The observation that the dynamics is well described by two frequencies calls for a modelling of the system as a pair of coupled oscillators. We then choose to describe the shell through two parameters, which naturally appear as relevant parameters in this problem: while the volume V is intimately related to the gas behaviour and is also the usual control or output parameter in shell buckling studies, the surface S appears in the stretching contribution of the elastic energy. While in the spherical case both parameters are interdependent, in the buckled state that introduces at least one more degree of freedom they can vary independently, as depicted in figure 5.
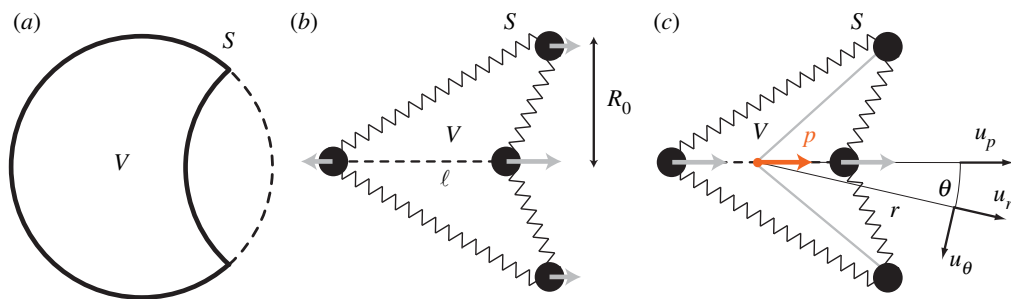
Figure 5. (*a*) Sketch of the parameters used to describe the shell dynamics. In addition to the volume *V*, we consider the surface *S* of the shell. In the buckled configuration, both can vary independently. The simplified view with springs and masses presented in (*b*,*c*) allows to model the flow field resulting from the variations of *V* and *S*. The Mises truss [50,51] is a convenient simplified model that has proven its efficiency to describe buckling dynamics of shallow arch [52] or elastic hemisphere (the 'jumping popper' toy) [14], in particular when the system is subjected to oscillating external forces. In this paper, we do not go further in the analogy that will be developed in subsequent papers, but we simply make the remark that in the three-dimensional shape obtained by axial rotation along the horizontal axis of the closed Mises truss depicted in (*b*) and (*c*), with the two lateral masses always located at fixed distance $2R_0$, *V* variations can be made while keeping *S* constant, as in (*b*), while in (*c*) surface variations are obtained while keeping *V* constant. This is obtained by a similar horizontal motion of both poles, keeping their interdistance ℓ constant. This results in an hydrodynamic dipole p at long range. Its intensity is related to the volume changes on each side of the mid-surface $S' = S/2$ indicated in grey. The assumption of fixed distance $2R_0$ between the two flanks is supported by the numerical simulations where we saw that most of the deformation occurs along the axis of symmetry (figure 2*h*). (Online version in colour.)

The modelling consists in writing how the elastic energy of the shell material and the potential energy of the inner gas depend on these two variables *V* and *S*, as well as the kinetic energy and the dissipation due to viscous friction.

(a) Potential energy

The potential energy can be written $U = U_g + U_{ext} + U_S$. The internal energy U_g of the gas reads, assuming an adiabatic behaviour:

$$U_g = \frac{P(V)V}{\kappa - 1} = \frac{P_0 V_0^\kappa}{(\kappa - 1)V^{\kappa - 1}}. \tag{4.2}$$

The term U_{ext} is the opposite of the work done by the external pressure on the shell, therefore

$$U_{ext} = P_{ext}V. \tag{4.3}$$

Finally, U_S is the elastic energy in the shell. For a given value of external pressure, equilibrium conditions $\partial L/\partial V = 0$ and $\partial L/\partial S = 0$ lead to the following set of equations that determine the equilibrium configuration (V_e, S_e):

$$P_{ext} - P(V_e) + \frac{\partial U_S}{\partial V}\big|_{(V_e, S_e)} = 0 \tag{4.4}$$

and

$$\frac{\partial U_S}{\partial S}\big|_{(V_e, S_e)} = 0. \tag{4.5}$$

As recalled before, at equilibrium the pressure difference $P_{ext} - P$ quasi-plateaus to a constant ΔP_{pl} as a function of equilibrium volumes V_e. The plateau pressure ΔP_{pl} depends on shell elastic properties and thickness over radius ratio. While there is to our knowledge no available theoretical expression for it, an ad-hoc expression was proposed in [29] based on numerical simulations.

Buckling is the mechanism by which the compressed spherical shell switches into an energetically more favourable configuration. Since bending energy is located in the rim, one can consider in a first approximation that at equilibrium, the surface in the buckled state is not compressed, as shown in figure 3a, where the surface area at equilibrium is only 5% lower than the initial one. In the scheme of figure 5a, it corresponds to an inversion of the right spherical cap towards the left pole. This implies that we can consider in first approximation that $S_e = 4\pi R_0^2$, independently from V_e. As a consequence of this and of the existence of the plateau pressure ΔP_{pl}, $\partial^2 U_S / \partial V^2|_{(V_e, S_e)} = 0$. This assumption has been validated afterwards by letting the above partial derivative be a free parameter in the fitting procedure of the data, which eventually lead to very small values compared with the other elastic constants of the problem. Around an equilibrium configuration, the elastic energy of the shell finally reads

$$U_S = U_S(V_e, S_e) - \Delta P_{pl}(V - V_e) + A_{VS}(V - V_e)(S - S_e) + \tfrac{1}{2}A_{SS}(S - S_e)^2, \tag{4.6}$$

where $A_{VS} = \partial^2 U_S / \partial V \partial S|_{(V_e, S_e)}$ and $A_{SS} = \partial^2 U_S / \partial S^2|_{(V_e, S_e)}$. These parameters depend, a priori, on the equilibrium state.

As discussed above, we expect the variations of elastic energy with S to be that of the stretching energy in the spherical case, since the curvature energy is localized in the rim. The elastic energy for a sphere of radius R can be directly obtained from the general expressions that are recalled in appendix B (equations (B6) and (B7)):

$$\left. \begin{aligned} U_{S,\text{sph}} &= U_{\text{stretch}} + U_{\text{bend}}, \text{ with} \\ \text{and} \qquad U_{\text{stretch}} &= 8\pi K_A \left(1 - \frac{R}{R0}\right)^2 R^2 \text{ and } U_{\text{bend}} = 8\pi K_B \left(1 - \frac{R}{R0}\right)^2. \end{aligned} \right\} \tag{4.7}$$

We have introduced the area bulk modulus $K_A = dE$ and the bending stiffness $K_B = d^3E/9$. From $d^2 U_{\text{stretch}}/dS^2|_{S_e} = Ed/S_e$ in the spherical case, we therefore postulate that $A_{SS} = Ed/S_e$.

Similar reasoning is not possible for A_{VS}, as V and S are interdependent in the spherical case. We simply assume that the scaling $A_{VS} = Ed/V_e \, k_{VS}$, where k_{VS} is a dimensionless constant, will capture the dependency with space variables. Since there are two relevant space variables that are R_0 (or S_e) and V_e, other scalings could be possible. Complementary tests with the general scaling $A_{VS} = Ed/(V_e^\beta R_0^{3(1-\beta)})k_{VS}$ while proceeding with the fitting procedure of the data according to the model have indeed shown that $\beta \simeq 1$ is the best choice.

(b) Kinetic energy

We now turn to the determination of the kinetic energy T. The determination of the fluid flow around the oscillating shell is a complex problem, for which we only consider the long distance solution, obtained by adding the contributions of the constant surface and of the constant volume motions of the shell.

Far from the shell (i.e. neglecting the shape details), shell volume variations lead to a flow induced by a point source, imposing a flow rate $q = \dot{V}$. By incompressiblity of the fluid, one obtains a first (radial) contribution $\mathbf{v}_1$ to the fluid velocity:

$$\mathbf{v}_1 = \frac{\dot{V}}{4\pi r^2} \mathbf{u}_r. \tag{4.8}$$

Determining the flow due to surface variations is more complex. We wish to establish its dependency with the two dynamical variables V and S. To that end, the geometry of the shell is simplified through an analogy with an axisymmetric spring-mass system, sketched in figure 5b,c.

As sketched in figure 5c, this simplification of the shell geometry leads to assimilate the deformation at constant volume to the synchronized motion of the two poles, thus considered as a

pair of source/sink of flow rates q' and $-q'$. This gives rise to an hydrodynamic dipole producing the flow field

$$\mathbf{v}_2 = \frac{2p\cos\theta}{4\pi r^3}\mathbf{u}_r + \frac{p\sin\theta}{4\pi r^3}\mathbf{u}_\theta, \tag{4.9}$$

where θ is the angle between $\mathbf{u}_p$ that points in the pole to pole direction and the radial unit vector $\mathbf{u}_r$, and $\mathbf{u}_\theta$ is the associated unit vector (figure 5c). The dipolar moment is $p = q'\ell$, where ℓ is the pole to pole distance. The dipolar approximation is well supported by the PIV observations made in [3], though it has been shown there that more complex patterns can take place due to shear waves near the flanks. The flow rate q' is related to the deformation of the shell. As we have symmetrized the problem in a first approximation, by considering that the source and the sink have the same absolute intensity, we relate the flow rate q' to the motion of the mid-surface (of area $S' = S/2$) going through the midpoint between the two poles, depicted in grey in figure 5c. As the poles move with velocity v_p, the rate of change of volume on each side of the mid-surface is $q'/2 = \pi R_0^2 v_p/3$. A bit of geometry gives the relation between the pole velocity v_p and the variation $\dot{S}'$ of the mid-surface, eventually leading to

$$q' = -\frac{R_0}{3}S(S^2 - 4\pi^2 R_0^4)^{-1/2}\dot{S}. \tag{4.10}$$

Finally, as $V = \pi R_0^2 \ell/3$, p can be written under the form $p = g(V,S)\dot{S}$ where $g(V,S) = -(VS/\pi R_0)(S^2 - 4\pi^2 R_0^4)^{-1/2}$.

Eventually, the kinetic energy is obtained by integrating $(1/2)\rho_f(\mathbf{v}_1 + \mathbf{v}_2)^2$ on the whole fluid volume Ω. By lack of knowledge on the effective shape, we integrate from R_0 to ∞ and compensate our successive approximations by introducing numerical prefactors α_1 and α_2 to the monopolar and dipolar terms, which we expect to be of order unity. They constitute the cost to pay in this simplified—then tractable—model.

We eventually obtain

$$T = \alpha_1 \rho_f \frac{\dot{V}^2}{8\pi R_0} + \alpha_2 \rho_f \frac{g(V,S)^2 \dot{S}^2}{12\pi R_0^3}. \tag{4.11}$$

(c) Dissipative function

The dissipative function D reads $D = \eta_f \int_\Omega (u_{ij})^2 \, dV$, where u_{ij} is the symmetric strain rate tensor in the fluid. We implicitly assume here that dissipation originates from viscous friction and that pressure drag is negligible; this is the framework in which the Rayleigh dissipative function has been introduced and validated so far. From the above expression for the fluid velocity, D can be straightforwardly calculated and we find by integrating from R_0 to ∞

$$D = \beta_1 \frac{\eta_f}{2\pi} \frac{\dot{V}^2}{R_0^3} + \beta_2 \frac{6\eta_f}{5\pi} \frac{g(V,S)^2 \dot{S}^2}{R_0^5}, \tag{4.12}$$

where the β_i have been introduced, as α_i for the kinetic energy, to account for the lack of precision in the integration domain.

(d) Dynamics around equilibrium

We obtain the oscillation equations by considering only first order terms in $\Delta V = V - V_e$ and $\Delta S = S - S_e$ in the Lagrangian equation (4.1), using equations (4.2), (4.3), (4.6), (4.11), (4.12) and $g(V_e, S_e)^2 = 4V_e^2/(3\pi^2 R_0^2)$:

$$\alpha_1 \frac{\rho_f}{4\pi R_0}\Delta\ddot{V} = -\frac{\kappa P_e(V_e)}{V_e}\Delta V - \frac{Ed}{V_e}k_{VS}\Delta S - \beta_1\eta_f \frac{1}{\pi R_0^3}\Delta\dot{V} \tag{4.13}$$

and

$$\alpha_2 \frac{2\rho_f}{9\pi^3 R_0^5}V_e^2\Delta\ddot{S} = -\frac{Ed}{V_e}k_{VS}\Delta V - \frac{Ed}{4\pi R_0^2}\Delta S - \beta_2\eta_f \frac{16V_e^2}{5\pi^3 R_0^7}\Delta\dot{S}. \tag{4.14}$$

Together with the equilibrium conditions

$$P_{\text{ext}} - P_e = \Delta P_{pl} = \frac{E}{(3/4)^{0.75}}(2.34\,10^{-6} + 0.9(d/R_0)^{2.57}),$$

$$\text{(according to [29])} \tag{4.15}$$

and

$$P_0 V_0^\kappa = P_e V_e^\kappa, \tag{4.16}$$

that set P_e and V_e, these equations allow to determine the motion of the shell as a function of the initial pressure P_0 inside the shell, the external pressure P_{ext}, the initial shell radius R_0, its thickness d, Young's modulus E and the fluid density and viscosity ρ_f and η_f. The impact of the geometry differs for each term considered in the equations, where R_0 and V_e appear with different powers.

Switching to the dimensionless parameters, equations (4.13) and (4.14) become

$$\frac{\alpha_1}{4\pi}\Delta\ddot{\hat{V}} = -\frac{\kappa\hat{P}_e(\hat{V}_e)}{\hat{V}_e}\Delta\hat{V} - \frac{k_{VS}}{\hat{V}_e}\Delta\hat{S} - \hat{\eta}\,\frac{\beta_1}{\pi}\,\Delta\dot{\hat{V}} \tag{4.17}$$

and

$$\frac{2\alpha_2}{9\pi^3}\hat{V}_e^2\Delta\ddot{\hat{S}} = -\frac{k_{VS}}{\hat{V}_e}\Delta\hat{V} - \frac{1}{4\pi}\Delta\hat{S} - \hat{\eta}\,\frac{16\beta_2\hat{V}_e^2}{5\pi^3}\,\Delta\dot{\hat{S}}. \tag{4.18}$$

In most cases of interest (table 1), $\hat{\eta}$ is small. This means that the fluid does not influence the shell dynamics, which would simplify the design and optimization of such a system, as well as its modelling: we can consider $\hat{\eta}$ as a small parameter and look for solutions of equations (4.17) and (4.18) under the form $Ae^{(i\hat{\omega}_0 - \hat{\delta})t}$, where $\hat{\delta}$ is a small parameter, instead of a general form $A\,e^{i\hat{\omega}t}$ which would result in a complex quartic equation for $\hat{\omega}$. There are such non-trivial solutions of the equations of motions if and only if the determinant of the associated matrix is zero:

$$\left(\frac{\alpha_1}{4\pi}(i\hat{\omega}_0 - \hat{\delta})^2 + \frac{\kappa\hat{P}_e(\hat{V}_e)}{\hat{V}_e} + \hat{\eta}\,\frac{\beta_1}{\pi}\,(i\hat{\omega}_0 - \hat{\delta})\right)$$

$$\times\left(\frac{2\alpha_2}{9\pi^3}\hat{V}_e^2(i\hat{\omega}_0 - \hat{\delta})^2 + \frac{1}{4\pi} + \hat{\eta}\,\frac{16\beta_2\hat{V}_e^2}{5\pi^3}\,(i\hat{\omega}_0 - \hat{\delta})\right) - \left(\frac{k_{VS}}{\hat{V}_e}\right)^2 = 0. \tag{4.19}$$

Taking the leading order in $\hat{\delta}$ and $\hat{\eta}$ (which is the 0th order) of the real part of the above equation we obtain two eigenpulsations

$$\hat{\omega}_\pm^2 = \frac{9\pi^2\alpha_1 + 32\pi\alpha_2\kappa\,\hat{V}_e\,\hat{P}_e \pm \sqrt{(9\pi^2\alpha_1 - 32\pi\alpha_2\kappa\,\hat{V}_e\,\hat{P}_e)^2 + 2\,\alpha_1\alpha_2(48\pi^2\,k_{VS})^2}}{16\alpha_1\alpha_2\hat{V}_e^2}. \tag{4.20}$$

This constitutes the central result of this study. The leading order of the imaginary part of equation (4.19) gives the two relaxation times $\hat{\tau}_\pm = \hat{\delta}_\pm^{-1}$ associated with the two above pulsations. *A priori*, these two times can be different. Nevertheless, we directly make use of the observation that all obtained oscillation signals in the simulations are very well fitted by the sum of two sinusoidal functions damped by the same exponential function. Consequently, there is only one damping time. It can be shown that $\hat{\tau}_+ - \hat{\tau}_-$ is proportional to $5\alpha_2\beta_1 - 18\alpha_1\beta_2$, which is therefore taken to be 0. Injecting the obtained value of β_2 in the expression for $\hat{\tau} \equiv \hat{\tau}_\pm$, we obtain

$$\hat{\tau} = 2\frac{\alpha_1}{\beta_1}\hat{\eta}^{-1} \quad \text{that is,} \quad \tau = 2\frac{\alpha_1}{\beta_1}\frac{\rho_f}{\eta_f}R_0^2. \tag{4.21}$$

5. Discussion

(a) Oscillation frequencies

We discuss the agreement between the model and the simulations. According to these, for the maximal value explored $\hat{\eta} = 1.3$, the dynamics is fully damped. Below $\hat{\eta} = 0.13$, few oscillations are seen and we are only able to determine the frequency $\hat{\omega}_-$ that contributes the most to the signal. Below $\hat{\eta} = 0.013$ both frequencies can be accurately determined. This range corresponds also to the small damping limit that lead to equation (4.20). This equation suggests that $\hat{V}_e^2 \hat{\omega}_\pm^2$ plotted as a function of $\hat{V}_e \hat{P}_e$ follows a master curve. In figure 6, we follow this idea and find that indeed the data collapse reasonably on a single curve considering the large range of control parameters considered. The set of data for $\hat{V}_e^2 \hat{\omega}_-^2$ and $\hat{V}_e^2 \hat{\omega}_+^2$ are well fitted by the proposed equation (equation (4.20)), the free parameters being α_1, α_2 and k_{VS}.

Fitting the two frequencies together leads to $\alpha_1 = 3.6 \pm 3.5\%$, $\alpha_2 = 1.1 \pm 4.1\%$ and $k_{VS} = 0.23 \pm 6.6\%$. These are acceptable ranges: α_i larger than 1 was expected since it is intended to be a correction of the fact we have not included the fluid inside the sphere of radius R_0 in the calculation of the kinetic energy.

Interestingly, ω_-^2 vanishes for a finite pressure, which sets a stability limit of the buckled state, which is given by

$$\hat{V}_e \hat{P}_e = 4\pi \frac{k_{VS}^2}{\kappa}. \tag{5.1}$$

This provides the minimal pressure needed to maintain the buckled shape.

The physical meaning of the two frequencies is particularly clear in the large $\hat{P}_e$ limit. From equation (4.17), we see that ω_+ and ω_- can then be interpreted as the contributions of the (now decoupled) volume and surface oscillations, respectively. From equation (4.20), we obtain

$$\hat{\omega}_+^2 \underset{\hat{P}_e \to \infty}{\sim} \frac{4\pi\kappa\hat{P}_e}{\alpha_1 \hat{V}_e}. \tag{5.2}$$

Though this expression ressembles a Minnaert contribution, as in the model of Marmottant *et al.* [41], it indeed differs from it by a factor $R_0/(\alpha_1 R_e)$ and will be smaller in most cases, as illustrated in the next section.

The smallest pulsation ω_- becomes, in the large $\hat{P}_e$ limit:

$$\hat{\omega}_-^2 \underset{\hat{P}_e \to \infty}{\sim} \frac{9\pi^2}{8\alpha_2 \hat{V}_e^2}. \tag{5.3}$$

Contrary to the spherical case, where the remaining contribution at high pressure is that of the gas pressure, we end up here with the sole contribution of the shell material compressibility. The high pressure makes the whole shell incompressible, but the buckled geometry makes it possible for the surface to evolve independently, with its own associated stiffness A_{SS}. The equivalent picture is that of two springs in series, one of them becoming infinitely stiff: the dynamics is then given by the smooth one. This contrasts with the case of the spherical geometry, where the springs are in parallel (see equation (B 13)).

The above considerations help explain the behaviour shown in figure 4*b*: as $\hat{P}_0$ increases, $\hat{V}_e$ increases and equation (5.3) shows that the pulsation is eventually a decreasing function of the initial—or of the equilibrium—pressure. For fixed volume $\hat{V}_e$ and varying inner pressure, equation (5.3) tells us that the frequency converges towards a finite limit, thus explaining why it does not increase linearly with the pressure (as in the spherical case), as shown in figure 4*b*.

(b) 'Softening' of buckled shells

Our results demonstrate that the oscillation frequencies of a shell drop after it has buckled. This so-called 'softening' is illustrated in figure 7 where we compare the obtained frequencies with that of the spherical case before buckling and that proposed in [41] for the buckled case.
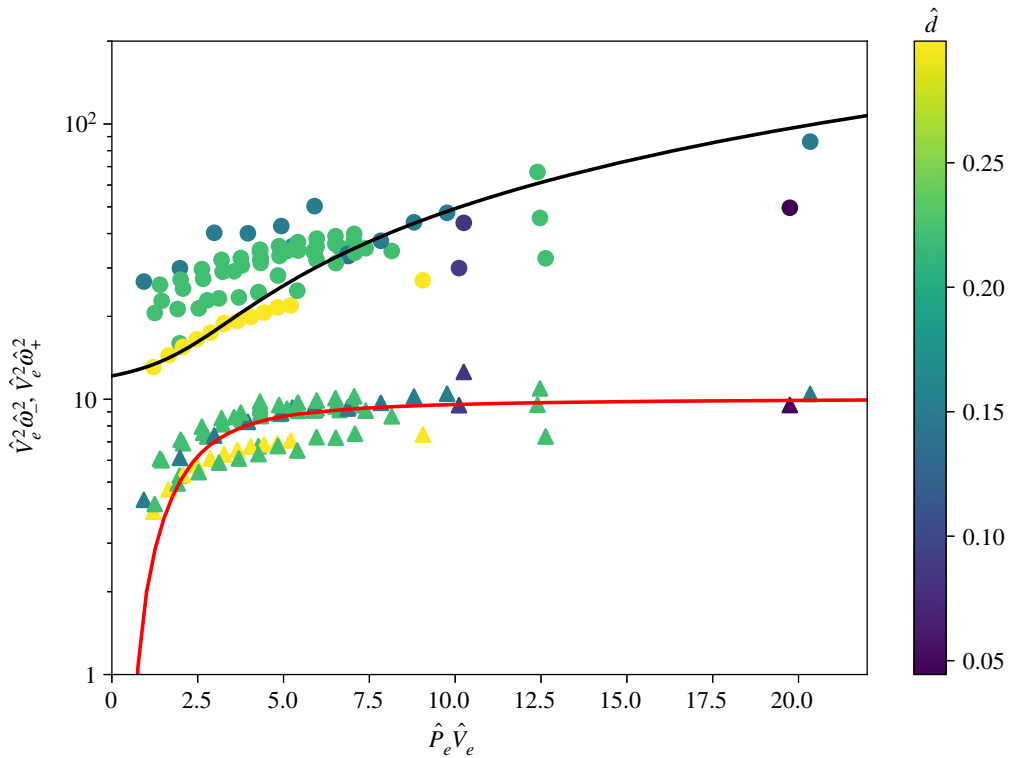
Figure 6. Dots : The two oscillations frequencies ω_- (triangles) and ω_+ (discs) as determined from the fit of the oscillations from numerical simulations. A joint fit of the two set of data by equation (4.20) leads to the full line curves. (Online version in colour.)

To do so, we consider increasing values of the external pressure P_{ext} starting at P_0 such that the shell is first in its spherical configuration until the pressure difference reaches the buckling pressure. In the buckled state, we consider either the Marmottant *et al.* model [41] or ours. The equilibrium configurations are calculated for each value of P_{ext}, with the internal pressure given by the adiabatic condition (equation (4.16)) and the resulting pressure difference being equilibrated by the elastic restoring force, which is given by equation (4.15) in the buckled case and by $-dU_{S,sph}/dV$ in the spherical case, where $U_{S,sph}$ is given by equation (4.7).

We show in particular that the 'softening' is characterized by a drop of the oscillation frequencies by factors 5 (for ω_-) and more than 2 (for ω_+) for parameters that are typical of the usual commercial UCAs, and is much more pronounced than that predicted in previous models, over a large range of parameters.

(c) Damping

The scaling of the damping time $\tau = 2(\alpha_1/\beta_1)(\rho_f/\eta_f)R_0^2$ predicted by equation (4.21) is the only one that can be built when considering only viscous effects in a fluid of density ρ_f, and viscosity η_f in the vicinity of an object of size R_0. Indeed, the assumption of viscous friction only was needed to calculate a dissipative function. It turns out that, due to the high Reynolds numbers that characterize the flow, this scaling does not hold in most of the considered range of parameters. We consider the Reynolds number based on the maximal flow velocity v_{pole} that is located near the buckling pole, which is then defined as $\mathcal{R}_e = v_{pole}R_0\rho_f/\eta_f$. As shown in figure 8, the dimensionless relaxation time $\eta_f\tau/(\rho_f R_0^2)$ indeed depends on the Reynolds number, while it would be constant if the dissipation was only of viscous origin (see equation (4.21)). The dependency with the
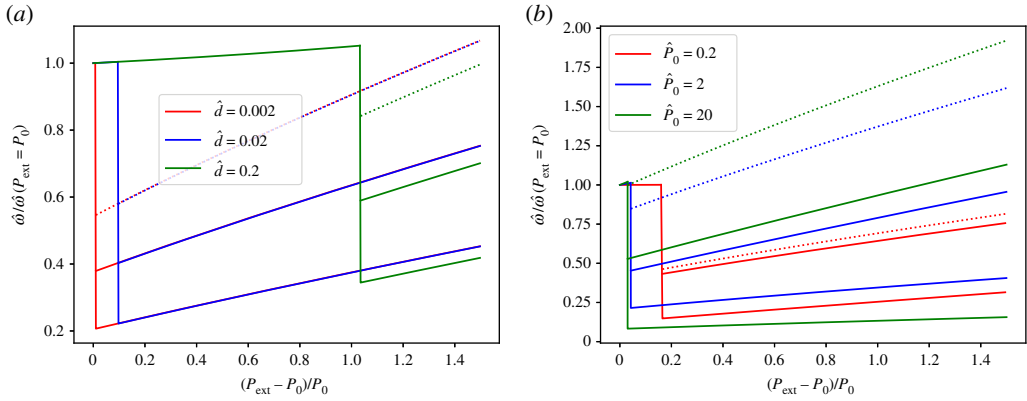
Figure 7. Oscillations frequencies around equilibrium position (normalized by that of the stress-free sphere) for several pairs of parameters $(\hat{d}, \hat{P}_0)$, as a function of applied external pressure $\hat{P}_{\text{ext}}$. (a) $\hat{P}_0 = 0.4$ fixed and varying $\hat{d}$. (b) $\hat{d} = 0.02$ fixed and varying $\hat{P}_0$. The low bounds correspond typically to commercial lipidic UCAs while the high bounds are relevant for soft polymeric shells, which are often thicker but made of a softer elastic material. Full lines indicate the single frequency in the spherical case (see equation (B13) in appendix B), and the two frequencies in the buckled case. Dotted lines correspond to the predictions in [41], where it is assumed that the pulsation is the Minnaert pulsation for the shell of radius R_0 at ambient pressure: $\omega = (1/R_0)\sqrt{3\kappa P_{\text{ext}}/\rho_f}$. (Online version in colour.)

Reynolds number is indeed pretty close (with no adjusted parameter) to that of the relaxation time towards constant velocity for a settling shell of radius R_0, for which the drag coefficient C_x is known [53]. This leads to the following general expression for the relaxation time:

$$\tau = \frac{8}{3} \frac{\rho_f R_0^2}{\eta_f C_x(\mathcal{R}_e)\mathcal{R}_e}. \tag{5.4}$$

The scaling of equation (4.21), which was valid only in the low Reynolds limit, is preserved, but a dependency of the prefactor with the Reynolds number must be introduced, in order to account for the hydrodynamics regime. In particular, in the heart of our space parameter of interest, the dissipation regime is thus that of the Allen regime [54], where a combination of viscous and pressure effects leads to a drag coefficient that roughly scales like $\mathcal{R}_e^{-0.6}$, in the $1 < \mathcal{R}_e < 10^3$ range.

As for the purely viscous case, considering the data for $\hat{\eta} = 0.13$, where $\mathcal{R}_e < 0.1$, equation (4.21) gives $\alpha_1/\beta_1 = 0.17$, quite close to the case of spherical oscillations where it would be equal to 0.125 according to [49].

We eventually make the remark that the model predicts that, for not too high $\hat{\eta}$—which will be the case in most situations—the frequencies scale with $1/R_0$, for a given reduced thickness d/R_0. This implies that the typical maximal velocity at the pole v_{pole}, which scales like ωR_0, is scale independent. In particular, on a large range of inner pressures, we can use the large pressure limit of equation (5.3) as an estimate for the leading frequency ω_-, leading to

$$v_{\text{pole}} \simeq \sqrt{\frac{9\pi^2 E(d/R_0)}{8\alpha_2\rho_f \hat{V}_e^2}}. \tag{5.5}$$

With typical values $E(d/R_0) = 1$ bar, $\rho_f = 1000$ kg m^{-3} and $\hat{V}_e = 1/2 \times 4\pi/3$, we find $v_p \sim 15$ m $\cdot$ s^{-1}. This implies that, even at small scales, the Reynolds number will be quite high, in the range 1–10^3 discussed above, which was obtained in the simulations.
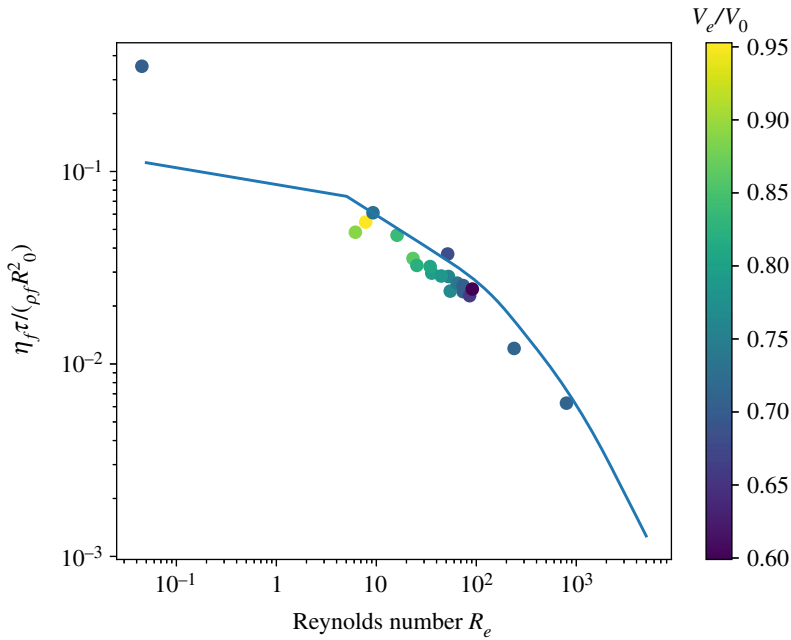
Figure 8. Theoretical oscillation relaxation time as a function of local Reynolds number (simulations). For a spherical bubble of radius R_0 settling in a fluid, the (velocity dependent) typical time needed to reach stationary velocity is $\eta_f \tau / (\rho_f R_0^2) = 8/(3C_x \mathcal{R}_e)$, where C_x is the drag coefficient [53] (that depends on $\mathcal{R}_e$) and $\mathcal{R}_e$ the Reynolds number. The full line indicates this quantity, which matches perfectly the measured damping time for the oscillations without any adjusted parameter. (Online version in colour.)

(d) Fixed shells: the effect of boundary conditions

In practical applications, a shell may be linked to other components. For our experiments on six different shells (see appendix A), buoyancy issues have required to restrict the displacement of the shell. For the three shells of external radii 7.5 mm, 25 mm and 75 mm, but identical $\hat{d}$ we checked the scalings $\omega \propto 1/R$. We have also simulated the same six shells in the same attachment conditions, assuming the part of the shell connected to the suction pad is fixed. In spite of this simplification, we find good agreement between the simulations and the experiments within 15% maximal variation for the measured frequencies, with no adjustable parameters.

In addition, these simulations show that the oscillation frequency is smaller by 25–50% than that of the free shell case. This is in qualitative agreement with the decrease of oscillation frequency of an initially free beam when it is attached at one end [19]. Yet this fact is not that intuitive since the attachment may lead to less fluid motion in the vicinity of the attachment patch, therefore less accelerated mass. Noteworthy, the additional local constraint also modifies the relative weights of the two sinusoidal responses, depending on the considered quantity (figure 9). While both frequencies are well present whatever the boundary condition when considering the volume oscillations, the picture is different when considering the oscillation of the height H of the shell or of its width W, as defined in figure 1. In particular, for the height, a single frequency becomes predominant in the attached case, as seen in figure 1 for the experiments. As a signature of robustness of the modelling, the same pair of frequencies is sufficient to describe the oscillations, whatever the considered quantity. A more systematic study of the dependency of each frequency on the boundary condition, and of its relative weight is the full signal, would require to define and parametrize the attachment area precisely. We simply conclude here that the two-oscillator modelling is a robust description that remains valid for shells with fixed parts.
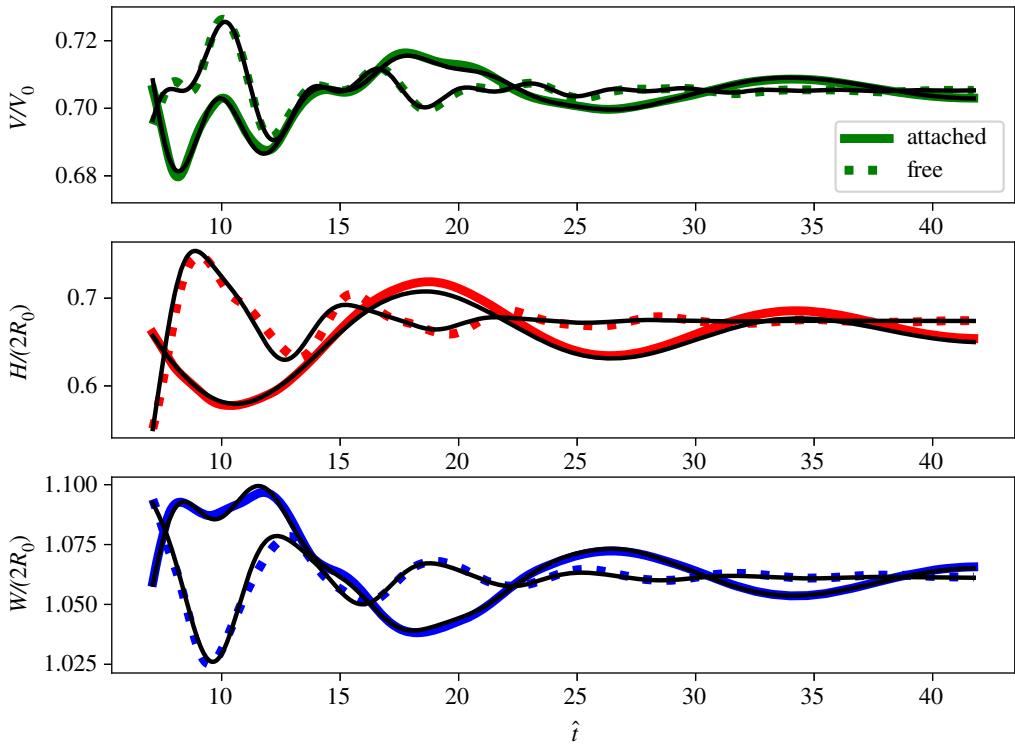
Figure 9. Oscillations of the volume V, height H and width W for a shell in configuration $\mathcal{R}$, which is attached or free (simulations). Thin black lines indicate the fit by the damped sum of two sinusoidal functions with the same frequencies ω_+ and ω_- for the three space variables. The amplitude ratio A_+/A_- of the two functions differs according to the variable considered. Free case: $\hat{\omega}_+ = 2.0$ and $\hat{\omega}_- = 1.0$; for V, $A_+/A_- = 0.52$, for H, $A_+/A_- = 0.21$, for W, $A_+/A_- = 0.22$. Attached case: $\hat{\omega}_+ = 1.6$ and $\hat{\omega}_- = 0.4$; for V, $A_+/A_- = 1.3$, for H, $A_+/A_- = 0.006$, for W, $A_+/A_- = 0.4$. (Online version in colour.)

6. Conclusion

In spite of the potentially huge number of deformation modes of a buckled shell, its dynamics can be described by a pair of coupled oscillators. The two resulting modes decouple in the high inner pressure limit and can be identified as the surface oscillation mode and the volume oscillation mode. The former corresponds to the lowest frequency and contributes more to the overall signal than the high frequency mode. Both frequencies are much lower than that in the spherical case. This confirms and quantifies the apparent softening of buckled shells observed in the literature. By contrast with previous models [41,42], we show that this softening is mainly due to the absence of contribution of the inner gas.

We have also shown that over a large range of parameters, the dissipation mechanism is similar to that of a sphere in translation in a fluid, whose drag coefficient is Reynolds-dependent.

The established model can be used to anticipate the behaviour of shells under more complex actuations than a fixed applied pressure. Using the model of Marmottant [41], it has recently been shown that buckling, by introducing an additional nonlinearity, may trigger complex dynamics characterized by subharmonic behaviour or even chaos [55]. More work is also needed to identify what controls the relative weight of each mode, and how this weight will be influenced by the boundary conditions, like local bonds to another component. We plan to dig in that direction in a near future. The model could also be further enriched by incorporating the contribution of the bending energy, which may help improving the collapse of data of figure 6 since it would introduce another dependency with the shell thickness. This contribution is already included in

the description of equilibrium through the expression of the plateau pressure (equation (4.15)) but it is still poorly understood. Another open question is that of the viscous dissipation within the shell material.

Appendix A. Experimental set-up

As in [3], the spherical shells were realized by moulding two half hollow spheres made of commercial elastomer resin 'Dragon Skin$^{©}$ 30' (Smooth-on) of Young's modulus $E = 0.5$ MPa (measured by traction experiments at 5% elongation, as well as Poisson's ratio $\nu = 0.5$). Other experiments on this material have shown that it behaves linearly at least until 25% deformation rate [34], thus validating the use of a linear model in the simulation. The two halves were then glued together using the same material. Flat discs of diameter of order 20% the shell diameter and thickness around 4% the shell thickness were added at the pole of one of the two external moulds so as to create a weak point on one hemisphere, where buckling will systematically occur.

In order to explore the effect of size and of thickness over radius ratio, we have considered six different shells whose external radii $R_{ext,0}$ lie between 7.5 and 75 mm while their dimensionless thicknesses $d/(R_{ext,0} - d/2)$ are between 0.08 and 0.3. We cover one order of magnitude in size and the relative thickness was varied by a factor almost 4. Reaching broader ranges poses technical issues in the manufacturing process.

The shell under study was attached at the level of its pole opposite to the weak one to a fixed support and immersed in a $60 \times 60 \times 60$ cm tank in anodized aluminum with polycarbonate polymer windows that could bear pressure differences of $+2$ bar. The tank was filled with glycerol. Pressure variations were obtained with a pressure controller (OB1 by Elveflow) connected to the thin layer of air that was left in the tank on top of the liquid. Shell deformations were recorded using a fast camera. Pictures of an immersed grid of known characteristics allows to characterize the deformation of pictures due to window deformation by the overpressure. As in figure 1, the obtained images of the convex envelops of the shells are well contrasted and their contours could be directly extracted and analysed using home-made routines written in Python.

Appendix B. Numerical method

The problem is numerically solved with finite elements making usage of the finite element toolbox AMDiS [57]. An axisymmetric arbitrary Lagrangian–Eulerian (ALE) method is employed according to [58], where the membrane points move with the fluid velocity **v**. This movement is harmonically extended to the internal part of the grid using one of the mesh smoothing approaches presented in [58].

The shell is modelled as an infinitely thin axisymmetric elastic surface, immersed in a Newtonian viscous fluid of viscosity η_f and density ρ_f and filled with air. The hydrodynamics in the surrounding fluid Ω are governed by the Navier–Stokes equations. The pressure due to the internal air is implemented as boundary conditions on the shell surface Γ. Assuming axisymmetric flow conditions reduces the problem to a two-dimensional meridian x–r-domain,

describing half of the three-dimensional domain's cross section. The simulation domain is shown in figure 10. The problem in axisymmetric formulation reads [59,60]

$$\rho_f(\partial_t \mathbf{v} + \mathbf{v} \cdot \nabla \mathbf{v}) = \nabla \cdot \mathbf{S} + \mathbf{v}_{\text{axi}}, \quad \text{in } \Omega \tag{B 1}$$

$$\nabla \cdot \mathbf{v} + \frac{1}{r} v_r = 0, \quad \text{in } \Omega \tag{B 2}$$

$$\mathbf{S} = \eta_f(\nabla \mathbf{v} + \nabla \mathbf{v}^T) - P_f \mathbf{I} \quad \text{in } \Omega, \tag{B 3}$$

where $\mathbf{v} = (v_x, v_r)^T$ and P_f are the fluid velocity and fluid pressure, respectively. The axisymmetric terms read

$$\mathbf{v}_{\text{axi}} = \left(\frac{2\eta_f}{r^2} v_r + \frac{1}{r}(\mathbf{S} + P_f \mathbf{I}) \right) \cdot \begin{pmatrix} 0 \\ 1 \end{pmatrix}. \tag{B 4}$$

The elastic shell reacts to in-plane (stretching) and out-of-plane (bending) deformations, quantified by the stretching energy E_{stretch} and the bending energy E_{bend}. The stretching energy in an axisymmetric setting can be described in terms of the two principal stretches λ_1 and λ_2, which provide information about relative changes of surface lengths in lateral and circumferential direction, respectively. It is

$$\lambda_1 = \frac{\mathrm{d}s}{\mathrm{d}s_0} \quad \text{and} \quad \lambda_2 = \frac{r_S}{r_{S,0}}, \tag{B 5}$$

with the arc length parameter s of the interface curve Γ and the distance of the shell r_S to the symmetry axis. The subscript 0 refers to the quantities in initial state. The shell energies then read

$$E_{\text{bend}} = \int_\Gamma 2K_B(H - H_0)^2 \, \mathrm{d}A \tag{B 6}$$

and

$$E_{\text{stretch}} = \int_\Gamma \frac{K_A + K_S}{2}((\lambda_1 - 1)^2 + (\lambda_2 - 1)^2) + (K_A - K_S)(\lambda_1 - 1)(\lambda_2 - 1) \, \mathrm{d}A, \tag{B 7}$$

with area bulk modulus K_A, area shear modulus K_S, bending stiffness K_B, mean curvature H and spontaneous curvature H_0, which is the mean curvature in the initial state. These three quantities can all be calculated using Young's modulus E, the Poisson ratio ν (which will be set to 0.5) and the (initial) thickness d of the shell:

$$K_A = \frac{dE}{2(1 - \nu)}, \quad K_S = \frac{dE}{2(1 + \nu)}, \quad K_B = \frac{d^3 E}{12(1 - \nu^2)}. \tag{B 8}$$

The force exerted by the shell is composed of the sum of the first variations of these energies and of the force due to the pressure of the internal air. Note that our thin shell model is a simplification that is made for technical purpose, but the elastic model describes a shell of any thickness. Since the strains are small compared with the deformations of a thin shell, the in-plane force is linearized in λ_i (see [61], appendix). In-plane and out-of-plane forces read [58]

$$\frac{\delta E_{\text{bend}}}{\delta \Gamma} = 4K_B[\Delta_\Gamma(H - H_0) + (4H^2 - 2K_g)(H - H_0) - 2H(H - H_0)^2]\mathbf{n} \tag{B 9}$$

and

$$\frac{\delta E_{\text{stretch}}}{\delta \Gamma} = (2H\mathbf{n} - \nabla_\Gamma)[(K_A + K_S)(\lambda_1 - 1) + (K_A - K_S)(\lambda_2 - 1)] + \frac{2K_S}{R}(\lambda_2 - \lambda_1)\begin{pmatrix} 0 \\ 1 \end{pmatrix}, \tag{B 10}$$

where K_g is the Gaussian curvature.

For the contribution of internal pressure, we assume homogeneous air pressure P inside and use adiabatic gas theory to relate this pressure to the inner shell volume V by $P = P_0 (V_0/V)^\kappa$, where P_0 and V_0 denote the respective initial values, and $\kappa = 1.4$ by assumption of an adiabatic
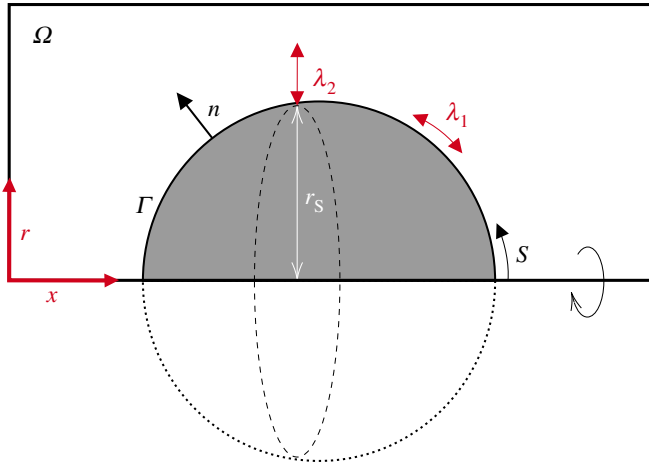
Figure 10. Numerical domain Ω for the simulations (white). The shell (dark grey) itself is not included. Γ is the domain boundary referring to the shell surface. Illustration for the principal stretches in red. (Online version in colour.)

process. Accordingly, the stress exerted by the air is reduced to $P\mathbf{n} = P_0 (V_0/V)^\kappa \mathbf{n}$ whereupon the boundary conditions become

$$\mathbf{Sn} = -P_0 \left(\frac{V_0}{V} \right)^\kappa \mathbf{n} - \frac{\partial E_{\text{bend}}}{\partial \Gamma} - \frac{\partial E_{\text{stretch}}}{\partial \Gamma} \quad \text{on } \Gamma \tag{B 11}$$

and

$$P_f = P_{\text{ext}} \quad \text{on } \partial\Omega \backslash \Gamma. \tag{B 12}$$

The numerical scheme in time step $m + 1$ can be summarized as follows. An implicit Euler method is employed for the Navier–Stokes equations. In the following, time steps indices are denoted by superscripts. The scheme reads:

(i) Calculate $\lambda_1, \lambda_2, H, K_g$ and $\mathbf{n}$ from the position of boundary grid points along Γ (see [58] for details). This allows computation of $(\delta E_{\text{stretch}}/\delta\Gamma)^{m+1}$ and $(\delta E_{\text{bend}}/\delta\Gamma)^{m+1}$ according to equations (B 9) and (B 10).
(ii) Solve the Navier–Stokes equations (B 1)–(B 4) of the surrounding fluid.
(iii) Move every grid point of Γ with velocity $\mathbf{v}$.
(iv) Calculate the grid velocity $\mathbf{v}_{\text{grid}}$ by using one of the mesh smoothing algorithms described in [58] to harmonically extend the interface movement into Ω and move all internal grid points of Ω with velocity $\mathbf{v}_{\text{grid}}$.

A function $P_{\text{ext}}(t)$ imposes variable pressure at the boundary $\partial\Omega \backslash \Gamma$ of the computational domain, excluding the shell (see equation (B 12)). The values for P_{ext} start for $t = 0$ at P_0. Afterwards, P_{ext} is increased slowly until the maximum desired value P_{max} is reached. The slow increase of pressure circumvents the occurrence of shell oscillations in the spherical compression stage before buckling. In order to analyse the post-buckling oscillations, the maximum pressure value is kept constant afterwards.

For the simulation results shown in figure 4, we first compute the equilibrium state after buckling as explained above. Then we impose an offset δP to both, the internal pressure P and the external pressure P_{ext}. The updated internal pressure acts as the new 'initial' pressure P_0 for the rest of the simulation. Subsequently, a perturbation to the shell is applied by adding another prescribed pressure P_{perturb} to the new P_{ext}. If the offset δP is zero, we could confirm that these oscillations, whose initial amplitude is smaller, are similar to those obtained right after the shell has buckled, which initially implies larger deformation.
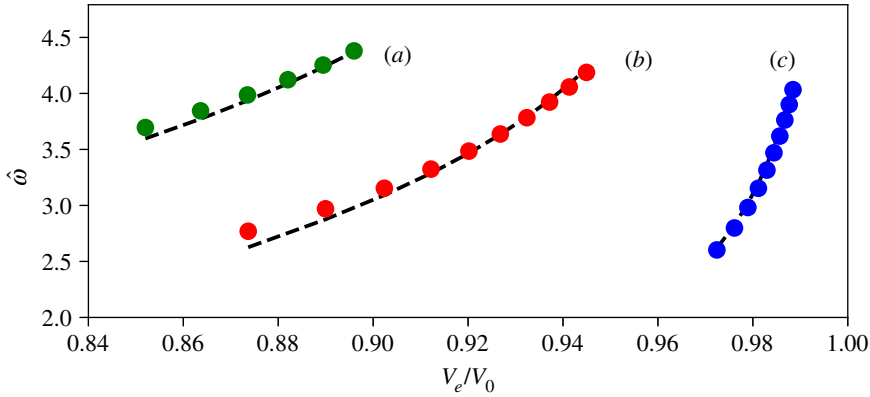
Figure 11. Pulsation $\hat{\omega}$ for spherical oscillation around equilibrium volume V_e, for the configuration $\mathcal{R}$ with varying initial pressures $\hat{P}_0$ that are equal inside and outside the shell and varying external pressure increases $\delta\hat{P}$; (a) and green: $\delta\hat{P} = 0.45$ and $0.9 < \hat{P}_0 < 1.8$; (b) and red: $\delta\hat{P} = 0.225$ and $0.18 < \hat{P}_0 < 1.8$; (c) and blue: $\delta\hat{P} = 0.045$ and $0.18 < \hat{P}_0 < 1.8$. The dashed lines indicate the best fit with equation (B13), where the pressure, geometric and elastic parameters are set to their values in the simulation and fixed, and the sole free parameter is a prefactor that will account for the mean error made in the simulation. (Online version in colour.)

A weak spot is imposed into the formula when calculating the elastic moduli K_A, K_S and K_B by decreasing the thickness d locally around the centre of the weak spot, which is the membrane point touching the symmetry axis ($r = 0$) on the right. This weak spot provides the perturbation needed to trigger buckling, otherwise our code is stable enough to let the shell stay in its spherical configuration, though unstable.

The oscillation frequencies are the main quantitative output of the simulations. They directly depend on the total accelerated mass and, because of that, the size of the simulation box may bias the results. To estimate this, we consider the spherical oscillations of the shell under low pressure difference, such that it has not buckled.

To that purpose, we considered simulations of the shell in configuration $\mathcal{R}$ but considered different initial pressure inside and outside the shell $\hat{P}_0$ going from 0.18 to 1.8. Then we applied suddenly an external pressure $\hat{P}_{\text{ext}} = \hat{P}_0 + \delta\hat{P}$ to the shell. For not too high values of $\delta\hat{P}$, the shell shrinks isotropically with damped oscillations towards its new configuration, characterized by an equilibrium volume $\hat{V}_e$.

The radial oscillations of a coated shell have been documented by several authors, for two-dimensional shells (thin shells) [41,62] and for real shell of finite thickness [36,49,56,63]. For two-dimensional shells, the expressions for the oscillation frequency that are proposed in the literature are generally obtained considering oscillations around the stress-free configuration of volume V_0. Here, we are interested in oscillations around any state, which results in a modified expression for the pulsation, which we derive hereafter. In addition, models for thin shells generally consider only the stretching energy, which scales with d, and discard the curvature energy, which scales with d^3. Here, in equation (4.7), we included both contributions in order to account for the oscillations of the mid-plane of shells of any thickness.

This elastic energy in the spherical configuration given in equation (4.7) can be rewritten in terms of V and V_0, and we can follow the Lagrangian formalism that has lead to equation (4.13). The pressure term is identical and the acceleration term can be calculated exactly by integrating the kinetic energy arising from the monopolar term from the equilibrium radius R_e to ∞.

The pulsation in the absence of damping then reads

$$\omega_{\text{sph}}^2 = \frac{1}{\rho_f R_e^2}\left[3\kappa P_e + \frac{4}{3}V_e^{-2/3}V_0^{-2/3}(4\pi K_b(2V_0^{1/3} - V_e^{1/3}) + (36\pi)^{1/3}K_a V_e^{1/3}(2V_e^{2/3} - V_0^{2/3}))\right].$$

(B 13)

In the absence of bending energy, and for oscillations around the stress-free state ($V_e = V_0$), we recover the usual expression [41,62] $\rho_f R_0^2 \omega_{\text{sph}}^2 = 3\kappa P_0 + 4K_a/R_0$.

In figure 11, we plot the obtained pulsations in the simulation and compare them with the expected values obtained from equation (B13). It is shown that the dependency with the shell parameters is recovered but the theoretical expression for ω_{sph} has to be multiplied by a prefactor 1.07 to obtain an agreement between numerical data and theory.

This means that while the physics is well described by the simulations, they lead to an overestimation of the pulsation by 7%. This overestimation factor does not depend on the chosen configuration so we associate it with the finite size of the simulation box Ω, which we checked by decreasing its size. The considered size in the paper is the result of a compromise between accuracy of the simulations and computation time.

References

1. Son K, Guasto J, Stocker R. 2013 Bacteria can exploit a flagellar buckling instability to change direction. *Nat. Phys.* **9**, 494–498. (doi:10.1038/nphys2676)
2. Huang W, Jawed MK. 2020 Numerical exploration on buckling instability for directional control in flagellar propulsion. *Soft Matt.* **16**, 604–613. (doi:10.1039/c9sm01843c)
3. Djellouli A, Marmottant P, Djeridi H, Quilliet C, Coupier G. 2017 Buckling instability causes inertial thrust for spherical swimmers at all scales. *Phys. Rev. Lett.* **119**, 224501. (doi:10.1103/PhysRevLett.119.224501)
4. Wischnewski C, Kierfeld J. 2020 Snapping elastic disks as microswimmers: swimming at low Reynolds numbers by shape hysteresis. *Soft Matter* **16**, 7088–7102. (doi:10.1039/D0SM00741B)
5. Gorissen B, Melancon D, Vasios N, Torbati M, Bertoldi K. 2020 Inflatable soft jumper inspired by shell snapping. *Sci. Robot.* **5**, eabb1967. (doi:10.1126/scirobotics.abb1967)
6. Gomez M, Moulton DE, Vella D. 2017 Passive control of viscous flow via elastic snap-through. *Phys. Rev. Lett.* **119**, 144502. (doi:10.1103/PhysRevLett.119.144502)
7. Rothemund P, Ainla A, Belding L, Preston DJ, Kurihara S, Suo Z, Whitesides GM. 2018 A soft, bistable valve for autonomous control of soft actuators. *Sci. Rob.* **3**, eaar7986. (doi:10.1126/scirobotics.aar7986)
8. Holmes DP, Crosby AJ. 2007 Snapping surfaces. *Adv. Mater.* **19**, 3589–3593. (doi:10.1002/adma.200700584)
9. Yang D, Mosadegh B, Ainla A, Lee B, Khashai F, Suo Z, Bertoldi K, Whitesides GM. 2015 Buckling of elastomeric beams enables actuation of soft machines. *Adv. Mater.* **27**, 6323. (doi:10.1002/adma.201503188)
10. Holmes DP. 2019 Elasticity and stability of shape-shifting structures. *Curr. Optim. Coll. Interf. Sci.* **40**, 118–137. (doi:10.1016/j.cocis.2019.02.008)
11. Stein-Montalvo L, Costa P, Pezzulla M, Holmes DP. 2019 Buckling of geometrically confined shells. *Soft Matt.* **15**, 1215–1222. (doi:10.1039/C8SM02035C)
12. Janbaz S, Bobbert FSL, Mirzaali MJ, Zadpoor AA. 2019 Ultra-programmable buckling-driven soft cellular mechanisms. *Mater. Horiz.* **6**, 1138–1147. (doi:10.1039/C9MH00125E)
13. Gomez M, Moulton DE, Vella D. 2017 Critical slowing down in purely elastic 'snap-through' instabilities. *Nat. Phys.* **13**, 142–145. (doi:10.1038/nphys3915)
14. Gomez M, Moulton DE, Vella D. 2019 Dynamics of viscoelastic snap-through. *J. Mech. Phys. Sol.* **124**, 781–813. (doi:10.1016/j.jmps.2018.11.020)
15. Sieber J, Hutchinson JW, Thompson JMT. 2019 Nonlinear dynamics of spherical shells buckling under step pressure. *Proc. R. Soc. A* **475**, 20180884. (doi:10.1098/rspa.2018.0884)
16. Carlson RL, Sendelbeck RL, Hoff N. 1967 Experimental studies of the buckling of complete spherical shells. *Exp. Mech.* **7**, 281. (doi:10.1007/BF02327133)
17. Hutchinson JW. 1967 Imperfection sensitivity of externally pressurized spherical shells. *ASME. J. Appl. Mech.* **34**, 49–55. (doi:10.1115/1.3607667)
18. Berke L, Carlson R. 1968 Experimental studies of the postbuckling behavior of complete spherical shells. *Exp. Mech.* **8**, 548. (doi:10.1007/BF02327517)
19. Landau L, Lifschitz E. 1986 *Theory of elasticity*, 3rd edn. Oxford, UK: Elsevier Butterworth-Heinemann.
20. Quilliet C, Zoldesi C, Riera C, van Blaaderen A, Imhof A. 2008 Anisotropic colloids through non-trivial buckling. *Eur. Phys. J. E* **27**, 13–20. (doi:10.1140/epje/i2007-10365-2)

21. Quilliet C, Zoldesi C, Riera C, van Blaaderen A, Imhof A. 2010 Erratum to: anisotropic colloids through non-trivial buckling. *Eur. Phys. J. E* **32**, 419–420. (doi:10.1140/epje/i2010-10633-0)

22. Knoche S, Kierfeld J. 2011 Buckling of spherical capsules. *Phys. Rev. E* **84**, 046608. (doi:10.1103/PhysRevE.84.046608)

23. Vliegenthart GA, Gompper G. 2011 Compression, crumpling and collapse of spherical shells and capsules. *New J. Phys.* **13**, 045020. (doi:10.1088/1367-2630/13/4/045020)

24. Quilliet C. 2012 Numerical deflation of beach balls with various Poisson's ratios: from sphere to bowl's shape. *Eur. Phys. J. E* **35**, 48. (doi:10.1140/epje/i2012-12048-3)

25. Knoche S, Kierfeld J. 2014 The secondary buckling transition: wrinkling of buckled spherical shells. *Eur. Phys. J. E* **37**, 62. (doi:10.1140/epje/i2014-14062-9)

26. Hutchinson JW, Thompson JMT. 2017 Nonlinear buckling behaviour of spherical shells: barriers and symmetry-breaking dimples. *Phil. Trans. R. Soc. A* **375**, 20160154. (doi:10.1098/rsta.2016.0154)

27. Zhang J, Zhang M, Tang W, Wang W, Wang M. 2017 Buckling of spherical shells subjected to external pressure: a comparison of experimental and theoretical data. *Thin-Walled Struct.* **111**, 58. (doi:10.1016/j.tws.2016.11.012)

28. Pezzulla M, Stoop N, Steranka MP, Bade AJ, Holmes DP. 2018 Curvature-induced instabilities of shells. *Phys. Rev. Lett.* **120**, 048002. (doi:10.1103/PhysRevLett.120.048002)

29. Coupier G, Djellouli A, Quilliet C. 2019 Let's deflate that beach ball. *Eur. Phys. J. E* **42**, 129. (doi:10.1140/epje/i2019-11900-2)

30. Li S, Matoz-Fernandez DA, Aggarwal A, Olvera de la Cruz M. 2021 Chemically controlled pattern formation in self-oscillating elastic shells. *Proc. Natl Acad. Sci. USA* **118**, e2025717118. (doi:10.1073/pnas.2025717118)

31. Quemeneur F, Quilliet C, Faivre M, Viallat A, Pépin-Donat B. 2012 Gel phase vesicles buckle into specific shapes. *Phys. Rev. Lett.* **108**, 108303. (doi:10.1103/PhysRevLett.108.108303)

32. Pitois O, Buisson M, Chateau X. 2015 On the collapse pressure of armored bubbles and drops. *Eur. Phys. J. E* **38**, 48.

33. Munglani G, Wittel FK, Vetter R, Bianchi F, Herrmann HJ. 2019 Collapse of orthotropic spherical shells. *Phys. Rev. Lett.* **123**, 058002. (doi:10.1103/PhysRevLett.123.058002)

34. Stein-Montalvo L, Holmes DP, Coupier G. 2021 Delayed buckling of spherical shells due to viscoelastic knockdown of the critical load. *Proc. R. Soc. A.* (doi:10.1098/rspa.2021.0253)

35. Helfield B. 2019 A review of phospholipid encapsulated ultrasound contrast agent microbubble physics. *Ultrasound Med. Biol.* **45**, 282–300. (doi:10.1016/j.ultrasmedbio.2018.09.020)

36. Chabouh G, Dollet B, Quilliet C, Coupier G. 2021 Spherical oscillations of encapsulated microbubbles: effect of shell compressibility and anisotropy. *J. Acoust. Soc. Am.* **149**, 1240–1257. (doi:10.1121/10.0003500)

37. Renaud G, Bosch JG, van der Steen AFW, de Jong N. 2015 Dynamic acousto-elastic testing applied to a highly dispersive medium and evidence of shell buckling of lipid-coated gas microbubbles. *J. Acoust. Soc. Am.* **138**, 2668–2677. (doi:10.1121/1.4932587)

38. Trivett D, Pincon H, Rogers P. 2006 Investigation of a three-phase medium with a negative parameter of nonlinearity. *J. Acoust. Soc. Am.* **119**, 3610–3617. (doi:10.1121/1.2197804)

39. Zaitsev V, Dyskin A, Pasternak E, Matveev L. 2009 Microstructure-induced giant elastic nonlinearity of threshold origin: mechanism and experimental demonstration. *Europhys. Lett.* **86**, 44005. (doi:10.1209/0295-5075/86/44005)

40. Memoli G, Baxter KO, Jones HG, Mingard KP, Zeqiri B. 2018 Acoustofluidic measurements on polymer-coated microbubbles: primary and secondary Bjerknes forces. *Micromachines* **9**, 404. (doi:10.3390/mi9080404)

41. Marmottant P, van der Meer S, Emmer M, Versluis M, de Jong N, Hilgenfeldt S, Lohse D. 2005 A model for large amplitude oscillations of coated bubbles accounting for buckling and rupture. *J. Acoust. Soc. Am.* **118**, 3499–3505. (doi:10.1121/1.2109427)

42. Sijl J, Overvelde M, Dollet B, Garbin V, de Jong N, Lohse D, Versluis M. 2011 'Compression-only' behavior: a second-order nonlinear response of ultrasound contrast agent microbubbles. *J. Acoust. Soc. Am.* **129**, 1729–1739. (doi:10.1121/1.3505116)

43. Marmottant P, Bouakaz A, de Jong N, Quilliet C. 2011 Buckling resistance of solid shell bubbles under ultrasound. *J. Acoust. Soc. Am.* **129**, 1231–1239. (doi:10.1121/1.3543943)

44. Errico C, Pierre J, Pezet S, Desailly Y, Lenkei Z, Couture O, Tanter M. 2015 Ultrafast ultrasound localization microscopy for deep super-resolution vascular imaging. *Nature* **527**, 499–502. (doi:10.1038/nature16066)

45. Segers T, Gaud E, Casqueiro G, Lassus A, Versluis M, Frinking P. 2020 Foam-free monodisperse lipid-coated ultrasound contrast agent synthesis by flow-focusing through multi-gas-component microbubble stabilization. *Appl. Phys. Lett.* **116**, 173701. (doi:10.1063/5.0003722)

46. Vilov S, Arnal B, Bossy E. 2017 Overcoming the acoustic diffraction limit in photoacoustic imaging by the localization of flowing absorbers. *Opt. Lett.* **42**, 4379–4382. (doi:10.1364/OL.42.004379)

47. Boughzala M, Stephan O, Bossy E, Dollet B, Marmottant P. 2021 Polyhedral Bubble Vibrations. *Phys. Rev. Lett.* **126**, 054502. (doi:10.1103/physrevlett.126.054502)

48. Strasberg M. 1953 The pulsation frequency of nonspherical gas bubbles in liquids. *J. Acoust. Soc. Am.* **25**, 536–537. (doi:10.1121/1.1907076)

49. Doinikov AA, Dayton PA. 2006 Spatio-temporal dynamics of an encapsulated gas bubble in an ultrasound field. *J. Acoust. Soc. Am.* **120**, 661–669. (doi:10.1121/1.2215228)

50. Huang N. 1972 Dynamic buckling of some elastic shallow structures subject to periodic loading with high frequency. *Int. J. Sol. Struct.* **8**, 315–326. (doi:10.1016/0020-7683(72)90092-3)

51. Ario I. 2004 Homoclinic bifurcation and chaos attractor in elastic two-bar truss. *Int. J. Non-Lin. Mech.* **39**, 605–617. (doi:10.1016/S0020-7462(03)00002-7)

52. Wiebe R, Virgin LN, Stanciulescu I, Spottswood SM, Eason TG. 2012 Characterizing dynamic transitions associated with snap-through: a discrete system. *J. Comput. Nonlinear Dynam.* **8**, 011010. (doi:10.1115/1.4006201)

53. Almedeij J. 2008 Drag coefficient of flow around a sphere: Matching asymptotically the wide trend. *Powder Technol.* **186**, 218–223. (doi:10.1016/j.powtec.2007.12.006)

54. Goossens WR. 2019 Review of the empirical correlations for the drag coefficient of rigid spheres. *Powder Technol.* **352**, 350–359. (doi:10.1016/j.powtec.2019.04.075)

55. Sojahrood AJ, Haghi H, Porter TM, Karshafian R, Kolios MC. 2021 Experimental and numerical evidence of intensified non-linearity at the microscale: the lipid coated acoustic bubble. *Phys. Fluids* **33**, 072006. (doi:10.1063/5.0051463)

56. Church CC. 1995 The effects of an elastic solid surface layer on the radial pulsations of gas bubbles. *J. Acoust. Soc. Am.* **97**, 1510. (doi:10.1121/1.412091)

57. Vey S, Voigt A. 2007 AMDiS: adaptive multidimensional simulations. *Comput. Visualization Sci.* **10**, 57–67. (doi:10.1007/s00791-006-0048-3)

58. Mokbel M, Aland S. 2020 An ALE method for simulations of axisymmetric elastic surfaces in flow. *Int. J. Numer. Meth. Fluids* **92**, 1604–1625. (doi:10.1002/fld.4841)

59. Mokbel D, Abels H, Aland S. 2018 A phase-field model for fluid-structure interaction. *J. Comput. Phys.* **372**, 823–840. (doi:10.1016/j.jcp.2018.06.063)

60. Kim J. 2005 A diffuse-interface model for axisymmetric immiscible two-phase flow. *Appl. Math. Comput.* **160**, 589–606. (doi:10.1016/j.amc.2003.11.020)

61. Mokbel M, Mokbel D, Mietke A, Träber N, Girardo S, Otto O, Guck J, Aland S. 2017 Numerical simulation of real-time deformability cytometry to extract cell mechanical properties. *ACS Biomater. Sci. Eng.* **3**, 2962–2973. (doi:10.1021/acsbiomaterials.6b00558)

62. de Jong N, Hoff L, Skotland T, Bom N. 1992 Absorption and scatter of encapsulated gas filled microspheres: theoretical considerations and some measurements. *Ultrasonics* **30**, 95–103. (doi:10.1016/0041-624X(92)90041-J)

63. Hoff L, Sontum PC, Hovem JM. 2000 Oscillations of polymeric microbubbles: effect of the encapsulating shell. *J. Acoust. Soc. Am.* **107**, 2272–2280. (doi:10.1121/1.428557)